Article

Polarization and Dielectric Properties of BiFeO₃-BaTiO₃ Superlattice-Structured Ferroelectric Films

Yuji Noguchi [1],* and Hiroki Matsuo [2],*

[1] Division of Information and Energy, Faculty of Advanced Science and Technology, Kumamoto University, 2-39-1, Kurokami, Chuo-ku, Kumamoto 860-8555, Japan
[2] International Research Organization for Advanced Science & Technology (IROAST), Kumamoto University, 2-39-1, Kurokami, Chuo-ku, Kumamoto 860-8555, Japan
* Correspondence: yuji19700126@gmail.com (Y.N.); matsuo_h@cs.kumamoto-u.ac.jp (H.M.)

Abstract: Superlattice-structured epitaxial thin films composed of Mn(5%)-doped BiFeO₃ and BaTiO₃ with a total thickness of 600 perovskite (ABO₃) unit cells were grown on single-crystal SrTiO₃ substrates by pulsed laser deposition, and their polarization and dielectric properties were investigated. When the layers of Mn-BiFeO₃ and BaTiO₃ have over 25 ABO₃ unit cells (N), the superlattice can be regarded as a simple series connection of their individual capacitors. The superlattices with an N of 5 or less behave as a unified ferroelectric, where the BaTiO₃ and Mn-BiFeO₃ layers are structurally and electronically coupled. Density functional theory calculations can explain the behavior of spontaneous polarization for the superlattices in this thin regime. We propose that a superlattice formation comprising two types of perovskite layers with different crystal symmetries opens a path to novel ferroelectrics that cannot be obtained in a solid solution system.

Keywords: perovskite; ferroelectric; polarization; dielectric; BiFeO₃; BaTiO₃; superlattice; film; epitaxial thin film

1. Introduction

Chemical tuning of the dielectric, ferroelectric, and piezoelectric properties of perovskite oxides (ABO₃) is traditionally based on the formation of solid solutions. Lead zirconate titanate, Pb(Zr, Ti)O₃, is representative, composed of ferroelectric PbTiO₃ in tetragonal symmetry, and antiferroelectric PbZrO₃ in rhombohedral symmetry [1,2]. In this system, the dielectric and piezoelectric properties are maximized near the composition-driven phase boundary [2], called the morphotropic phase boundary (MPB) [3], between the tetragonal and rhombohedral structures. The similar materials strategy has provided an extremely high piezoelectric response [4,5] in solid solutions such as Pb(Mg, Nb)O₃–PbTiO₃ and Pb(Zn, Nb)O₃–PbTiO₃, where an electric field (E) is considered to induce a rotation of spontaneous polarization (P_s) [6].

Recently, bismuth ferrite (BiFeO₃) [7,8] has attracted considerable attention because of its multiferroic nature [9,10], i.e., the simultaneous presence of ferroelectric P_s and an incommensurate spin cycloid structure, even at room temperature. Bulk BiFeO₃ has a rhombohedral structure in space group $R3c$ and possesses a large P_s along the pseudo-cubic [111]$_c$ direction [11,12]. Moreover, BiFeO₃ exhibits an extremely high Curie temperature (T_C) of 830 °C [11,12], which can provide piezoelectric devices operating at high temperatures. In analogy to Pb(Zr, Ti)O₃, considerable efforts have been made to investigate the solid solutions of rhombohedral BiFeO₃ and other perovskites in tetragonal symmetry. The BiFeO₃–BaTiO₃ system [13–17] has been widely studied mainly in ceramic form because the MPB is expected to appear between rhombohedral $R3c$ and tetragonal $P4mm$. Detailed structural analysis reveals that an increase in the BaTiO₃ content causes a structural change from rhombohedral $R3c$ to a pseudo-cubic structure [17], where the phase boundary is

ambiguous at around 33% BaTiO₃ content. Moreover, it has been reported that BiFeO₃–BaTiO₃ solid solutions do not have a ferroelectric nature in the BaTiO₃ content range of 40–50% [18].

Another approach exploiting the interplay of two types of perovskite oxides is to build a superlattice by thin-film growth technology [19,20]. Epitaxially grown superlattices composed of BiFeO₃ and BaTiO₃ have been reported to show a high magnetoelectric coupling coefficient compared with pristine films or bulk ceramics of BiFeO₃, where the interface plays a crucial role [21,22]. At present, ferroelectric and dielectric properties of BiFeO₃–BaTiO₃ superlattices have been reported in a few reports [23–25], and thereby the fundamental questions remain unanswered concerning how the layers of BiFeO₃ and BaTiO₃ are structurally and ferroelectrically coupled, and how the coupling of the two layers is activated.

In this paper, we report the crystal structure, polarization, and dielectric properties of superlattice-structured epitaxial thin films composed of BaTiO₃ and BiFeO₃ on single-crystal SrTiO₃ substrates prepared by pulsed laser deposition (PLD) (Figure 1). Here, we adopted Mn(5%)-doped BiFeO₃ instead of BiFeO₃ to avoid a considerable influence of oxygen vacancies on the polarization and leakage current properties [23,26–28], because a trapping capability of oxygen vacancies by Mn^{3+} at the Fe^{3+} site, i.e., a strong attractive interaction between Mn^{3+} and oxygen vacancy, inhibits the formation of an oxygen vacancy-rich layer at the interfaces. The total number of ABO₃ unit cells were fixed at 600, and that of the BaTiO₃ and Mn-BiFeO₃ layers (N) varied from 300 down to 1 (Figure 1b), while the average composition of the entire superlattices remained unchanged, i.e., 50% Mn-BiFeO₃–50% BaTiO₃. We found that the samples for an N greater than 25 can be regarded as a simple series connection of their individual capacitors, while those for an N of 5 or less behave as a unified 'ferroelectric', where the BaTiO₃ and Mn-BiFeO₃ layers are structurally and electronically coupled.
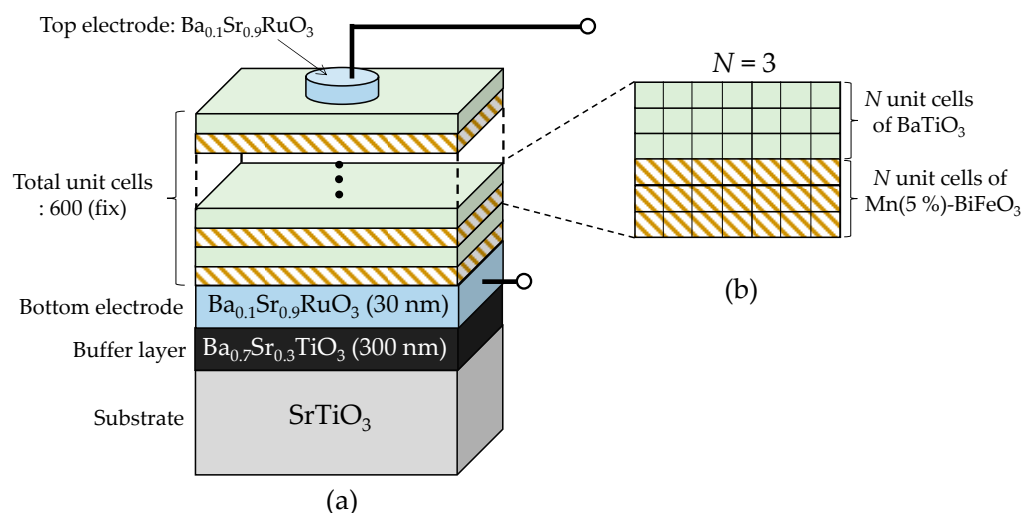
Figure 1. Schematics of the superlattice-structured thin film composed of layers of Mn(5%)-doped BiFeO₃ and BaTiO₃. The total thickness of the superlattice is fixed at 600 ABO₃ unit cells (**a**), and the number (N) of ABO₃ in the two layers varies from 300 to 1, see (**b**) for N = 3.

2. Materials and Methods

2.1. Experimental

Thin films of BaTiO₃ [29] and Mn(5%)-doped BiFeO₃ [28,30], a (Ba₀.₇Sr₀.₃)TiO₃ buffer layer [29], and (Ba₀.₁Sr₀.₉)RuO₃ electrodes [31] were fabricated on (100) SrTiO₃ single-crystal substrates (5 × 5 × 1 mm³) by PLD (KrF excimer laser, λ = 248 nm) using ceramic targets. The details of the deposition conditions are summarized in Supplementary Tables S1 and S2. Figure 1 displays the schematic of the superlattice composed of Mn-BiFeO₃ and BaTiO₃. The total number of ABO₃ unit cells was fixed at 600 (Figure 1a). The number

(*N*) of those in each layer forming the superlattice varied: *N* = 300, 50, 25, 10, 5, 3, and 1. Figure 1b depicts the structure of *N* = 3 as an example, where the superlattice is constructed by an alternate stacking of the thin layers of $BaTiO_3$ and Mn-$BiFeO_3$ with three ABO_3 unit cells (*N* = 3). For all the samples, the Mn-$BiFeO_3$ layer was deposited on the bottom electrode because of its better in-plane lattice matching with it. As a result, the layer just beneath the top electrode was the $BaTiO_3$ layer. During the deposition, the following condition was adopted: a substrate temperature T_{sub} of 640 °C, an oxygen pressure (Po_2) of 2.6 Pa, and a laser repetition rate of 1 Hz for $BaTiO_3$ and 7 Hz for Mn-$BiFeO_3$. The diameter of the top electrode was 0.1 mm. The polarization electric field (*P-E*) hysteresis properties were measured at 25 °C (3 kHz); the direction from the bottom to the top electrode was defined as positive for *E* and *P*.

High-resolution X-ray diffraction (XRD) reciprocal space maps (RSMs) were observed by using a Cu-$K\alpha_1$ source. The data of the intensity profile $I_i(q_x, q_z)$ of reflection *i* in the reciprocal space (q_x, q_z) were used for the detailed analysis of the lattice parameters of the in-plane (*a*) and the out-of-plane (*c*) directions, where the parameters *a* and *c* denote those of the pseudo-cubic ABO_3 unit cell. Throughout this paper, we adopted the pseudo-cubic notation unless otherwise stated.

2.2. DFT Calculations

Density functional theory (DFT) calculations were conducted using the generalized gradient approximation [32] with a plane wave basis set. We used the projector-augmented wave method [33] as implemented in the Vienna ab initio simulation package (VASP) [34]. We employed the Perdew–Burke–Ernzerhof gradient-corrected exchange correlation functional revised for solids (PBEsol) [35] and a plane wave cut-off energy of 520 eV. A Γ centered *k*-point mesh was used, and the details are provided later. Within the simplified generalized gradient approximation (GGA)+*U* approach [36], we added on-site Coulomb interaction parameters of $U−J$ of 6 eV to Fe-3*d* throughout the calculations. As the spin configuration in $BiFeO_3$ can be approximated as the G-type antiferromagnet [37], we set the spin arrangement in which the adjacent Fe ions have an antiparallel spin configuration as much as possible. The experimental results for Mn-doped $BiFeO_3$ films reveal that the crystal symmetry and the spontaneous polarization (P_s) are not influenced by the doping of Mn up to 10%, and therefore we considered $BiFeO_3$ instead of Mn-doped $BiFeO_3$ for simplicity.

For building a superlattice cell, we took the following lattice constraint. Based on the experimental results of XRD for an *N* of 5 or less, the superlattice cell had a tetragonal structure with the lattice parameters of in-plane a_{DFT} and out-of-plane c_{DFT} in space group *P*4*mm*; its a_{DFT} was fixed at the experimental *a* of 0.3985 nm, i.e., a_{DFT} = *a* (experiment). The parameter c_{DFT} is given by the following equation, $c_{DFT} = Nc_{BiFeO_3} + Nc_{BaTiO_3}$, where c_{BiFeO_3} denotes the parameter *c* of the $BiFeO_3$ unit cell, and c_{BaTiO_3} that of the $BaTiO_3$ unit cell. The c_{BiFeO_3} and c_{BaTiO_3} were determined from the lattice volumes (*V*) derived from the geometrical optimizations of the $BaTiO_3$ cell (5 × 5 × 5 *k*-point) and the $BiFeO_3$ cell in *P*4*mm* symmetry. Considering the antiparallel spin configuration, we performed the optimization calculation of the $BiFeO_3$ cell with $2c_{BiFeO_3}$ (5 × 5 × 3 *k*-point) and regarded the half cell with c_{BiFeO_3} as the $BiFeO_3$ unit cell. For imposing the antiparallel spin configuration for *N* = 1, the long lattice with $2c_{super}$ was taken as the superlattice cell, as depicted in Figure 2a. The structural optimizations were performed under a fixed a_{DFT} and c_{DFT} with 5 × 5 × 3 *k*-point mesh for all the supercells. From the structural parameters of the optimized cell, we obtained the atomic displacements (Δz) from the corresponding positions in the hypothetical non-polar paraelectric lattice. We also calculated the Born effective charges (Z^*) [38] in the superlattice cells by density-functional perturbation theory. We estimated P_s, as expressed by the following equation:

$$P_s = \sum_i m_i \cdot \Delta z_i \cdot Z_i^* / V, \tag{1}$$

where m_i denotes the site multiplicity of the constituent atom i, and $\Delta z_i \cdot Z_i^*$ is its dipole moment. The summation in Equation (1) is taken over the superlattice cell with the cell volume (V).
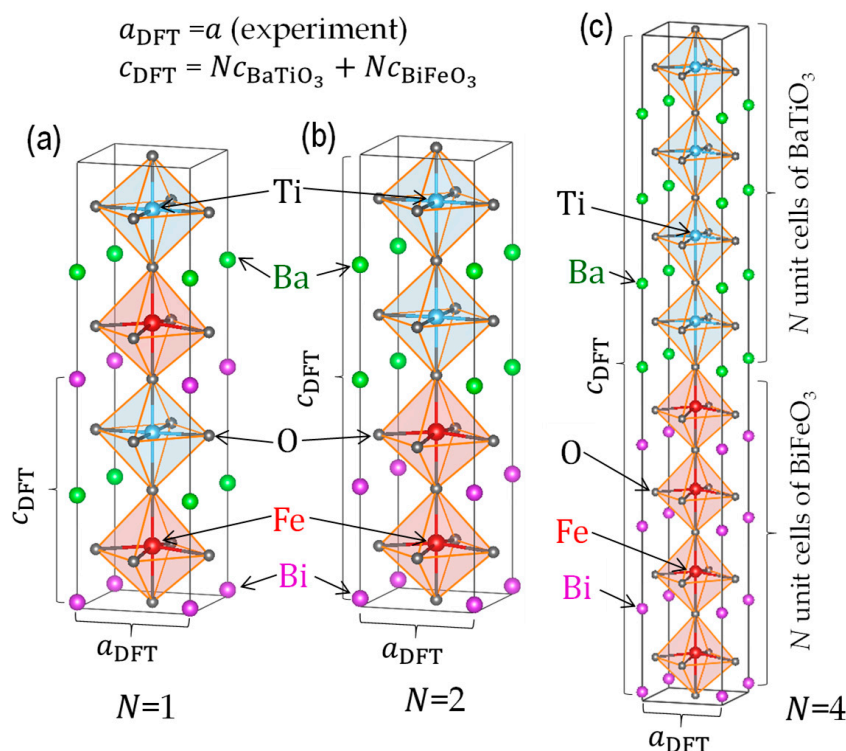
Figure 2. Crystal structures of the superlattice cells with (**a**) $N = 1$, (**b**) $N = 2$, and (**c**) $N = 4$ obtained from the structural optimizations by DFT calculations, where $BiFeO_3$ is employed instead of Mn-$BiFeO_3$ for simplicity. The in-plane lattice parameter a_{DFT} of the superlattice cell was fixed at the experiment: a (experiment) = 0.3985 nm. The out-of-plane lattice parameter c_{DFT} of the superlattice cell was determined from the cell volume obtained by geometrical optimizations in our preceding calculations of $BiFeO_3$ and $BaTiO_3$ in tetragonal *P4mm* symmetry.

## 3. Results

3.1. Crystal Structure

Supplementary Figure S1 shows the θ-2θ XRD patterns around the 002 reflection. In addition to the peaks of the $SrTiO_3$ substrate at 46.5°, the $(Ba_{0.1}Sr_{0.9})RuO_3$ electrodes at 46.4°, and the $(Ba_{0.7}Sr_{0.3})TiO_3$ buffer at 44.7°, the sample with $N = 300$ exhibits peaks individual to the layers of $BaTiO_3$ and Mn-$BiFeO_3$ because their layers are sufficiently thick for providing their corresponding reflections. With decreasing N, the integrated intensities of these peaks are weakened and eventually vanish for an N less than 5.

Supplementary Figure S2 shows the wide-area XRD-RSMs for $N = 300$ and 5. For $N = 300$ (Figure S2b), the apparent reflections of 3/2 3/2 1/2 and 1/2 1/2 3/2 of Mn-$BiFeO_3$ in monoclinic symmetry appear, whereas those were not observed for an N of 5 (Figure S2d) or less. Figure 3 shows the integrated intensity of the 1/2 1/2 3/2 reflection as a function of N. With decreasing N, the intensity is weakened and then zero for $N = 1$–5. These results indicate that the monoclinic distortion, similar to the bulk (rhombohedral), is maintained in the Mn-$BiFeO_3$ layer for the superlattice with $N \geq 10$, while that is lost with $N \leq 5$. The details of the structural analysis are described in Supplementary Note 2.

Figure 4 shows the high-resolution XRD-RSMs around the 103 reflections. For all the samples, the peak positions (q_x, q_z) exhibit the following features: the $(Ba_{0.7}Sr_{0.3})TiO_3$ buffer and the $(Ba_{0.1}Sr_{0.9})RuO_3$ electrodes have an apparently small q_x compared with the $SrTiO_3$ substrate, demonstrating that the parameter a of the $(Ba_{0.7}Sr_{0.3})TiO_3$ buffer is sufficiently expanded to the bulk value, and also that the $(Ba_{0.1}Sr_{0.9})RuO_3$ bottom electrode

is coherently grown on the buffer. The detailed structural analysis for $N = 300$ (Figure 4a along with the 113 reflection; see Supplementary Note 2) indicates that the Mn-BiFeO$_3$ layer has a rhombohedral-like monoclinic M_A structure. The splitting into two peaks of the 103 reflection of the Mn-BiFeO$_3$ layer stems from the ferroelastic domain variants. With further decreasing N, the splitting of the Mn-BiFeO$_3$ layer is smaller, and then the reflection can be regarded as a single peak for $N = 25$ and 10. At the same time, the q_z of the Mn-BFO layer with $N = 50$, 25, and 10 becomes larger than that of $N = 300$, suggesting a structural change from the M_A to monoclinic M_B phases owing to an in-plane tensile strain (see Supplementary Note 2). The experimental results, i.e., the single peak of the 103 reflection, the q_z shift, and the apparent 1/2 1/2 3/2 reflection (Figure 3), indicate that the Mn-BiFeO$_3$ layer for $N = 25$ and 10 has a pseudo-tetragonal structure, with a small monoclinic (M_B) distortion [39]. We note that for an N less than 5, the reflections from the Mn-BiFeO$_3$ and BaTiO$_3$ layers cannot be distinguished. These results enable us to consider that the superlattice has a unified tetragonal cell with a c/a of 1.01–1.02 as an average structure.
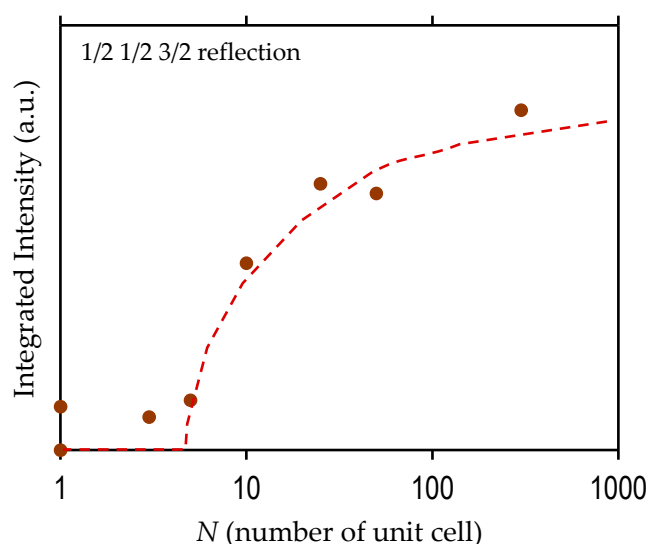

Figure 3. Integrated intensity of 1/2 1/2 3/2 reflection in the XRD-RSMs as a function of N, where N denotes the number of ABO$_3$ unit cells in the two layers of Mn-BiFeO$_3$ and BaTiO$_3$ comprising the superlattice. We confirmed that the integrated intensity of 1/2 1/2 3/2 reflection of the pristine Mn-BiFeO$_3$ film (300 unit cell thickness) is almost the same as that for $N = 300$.

3.2. Polarization and Dielectric Properteis

Figure 5 shows the *P-E* loops ($E//[001]_c$ at 3 kHz), and Figure 6a,b display the resultant remanent polarization (P_r) and the maximum polarization (P_{max}) at the highest positive E as a function of N, respectively. It is interesting to note that the superlattice samples exhibit an apparent ferroelectric polarization with an apparent P_r, which is completely different from the solid solutions in the same composition (50% BaTiO$_3$ content) featuring a non-ferroelectric nature [18]. The $N = 300$ sample has a P_r of 22 μC cm^{-2}. The *P-E* loop exhibits an imprint, i.e., a shift in the negative E direction. This behavior is assumed to stem from a flexoelectric effect [29,40,41], where a strain gradient in the out-of-plane direction in the ferroelectric layer stabilizes the upward polarization compared with the downward one. Compared with the buffered electrode with $a = 0.3986$ nm, the BaTiO$_3$ layer has the same a, whereas the Mn-BiFeO$_3$ layer possesses a slightly small $a = 0.3965$ nm. This result indicates that a strain gradient driving the flexoelectric effect is present in the Mn-BiFeO$_3$ layer adjacent to the boundary with the bottom electrode.
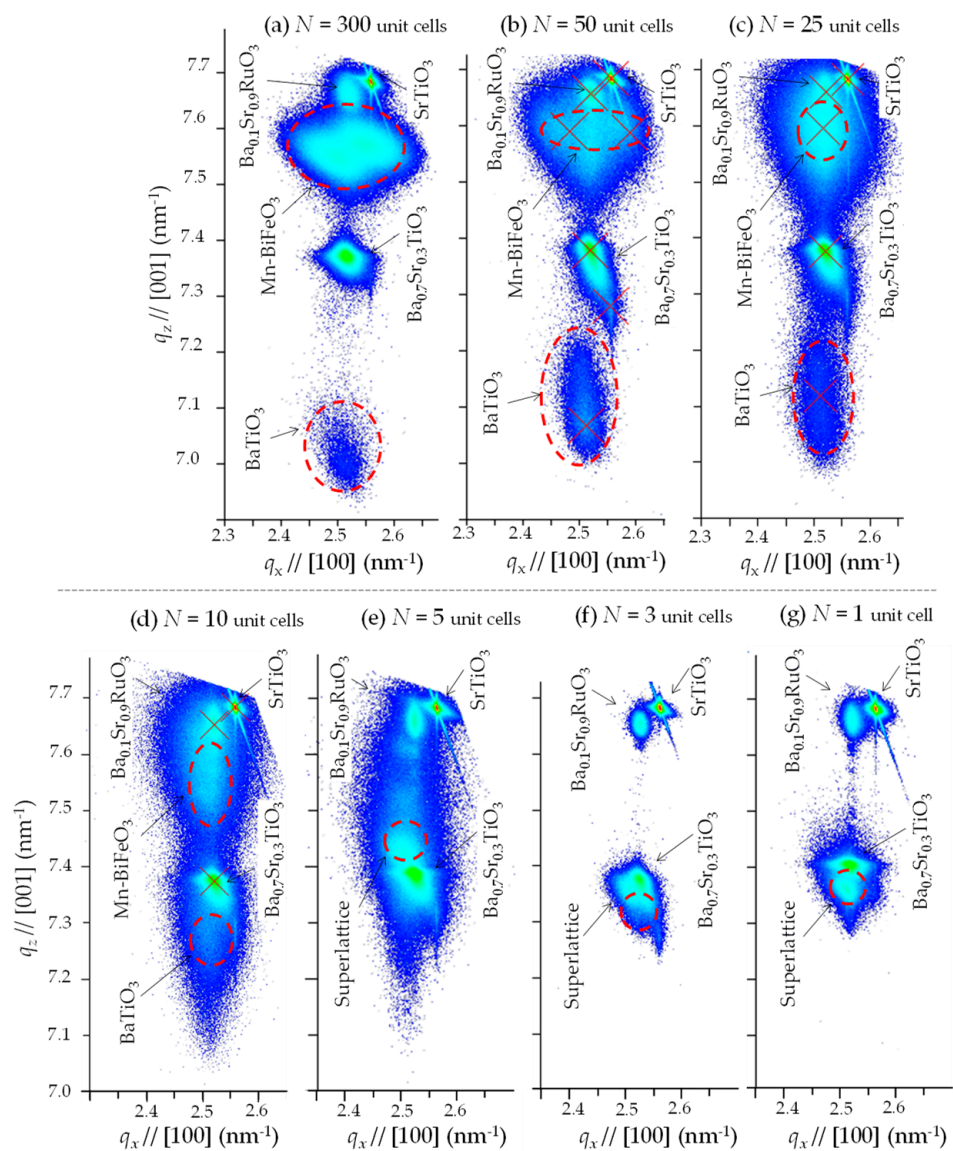
Figure 4. High-resolution XRD-RSMs around 103 reflection for (**a**) $N = 300$, (**b**) $N = 50$, (**c**) $N = 25$, (**d**) $N = 10$, (**e**) $N = 5$, (**f**) $N = 3$ and (**g**) $N = 1$, where the vertical axis is $q_z//[001]$ and the horizontal axis is $q_x//[100]$, where N denotes the number of ABO_3 unit cells in the two layers of Mn-BiFeO$_3$ and BaTiO$_3$ comprising the superlattice. Here, [001] and [100] are the crystallographic directions of the (100) SrTiO$_3$ substrate.

From the data shown in Figure 6a–c, we think that the polarization and dielectric behavior can be divided into three regions: I. the simple series connection of the capacitors ($N \geq 25$, see Figure 7a), II. the transition region ($10 \leq N < 25$), and III. the unified ferroelectric regime ($N < 10$, see Figure 7b). In region I, with decreasing N, the hysteresis is slanted, and the resultant P_r and P_{max} are monotonically reduced (Figure 6a,b). We note that the relative dielectric permittivity (ε_r) remains constant at ~120. This constant ε_r can be understood in terms of a simple series connection of the capacitors of the Mn-BiFeO$_3$ and the BaTiO$_3$ layers. Considering an ε_r of 399 for the Mn-BiFeO$_3$ capacitor, and that of 93 for the BaTiO$_3$ one (those were measured individually for their respective capacitors), we obtain ε_r~150 ($= 2\varepsilon_r(\text{BaTiO}_3) \cdot \varepsilon_r(\text{Mn-BiFeO}_3)/[\varepsilon_r(\text{BaTiO}_3) + \varepsilon_r(\text{Mn-BiFeO}_3)]$). This is qualitatively in good agreement with the experiment (ε_r~120). In region III, with decreasing N, the P_r is reduced, while the ε_r is higher.
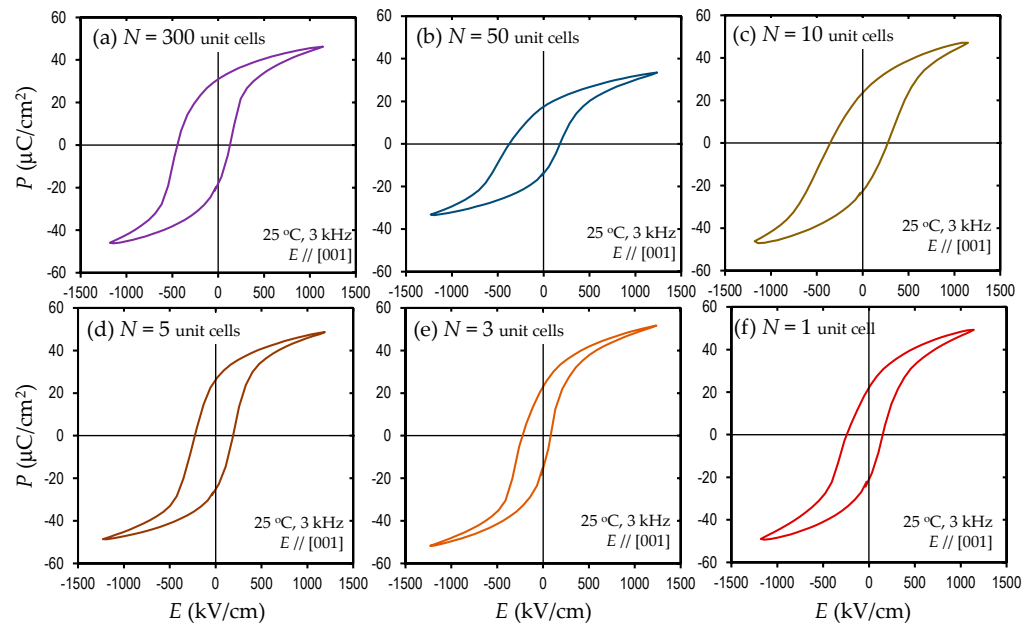
Figure 5. Polarization (P) electric field (E) hysteresis loops at 25 °C, for (**a**) $N = 300$, (**b**) $N = 50$, (**c**) $N = 10$, (**d**) $N = 5$, (**e**) $N = 3$ and (**f**) $N = 1$, where an E of 3 kHz is applied along [001], where N denotes the number of ABO_3 unit cells in the two layers of Mn-$BiFeO_3$ and $BaTiO_3$ comprising the superlattice.
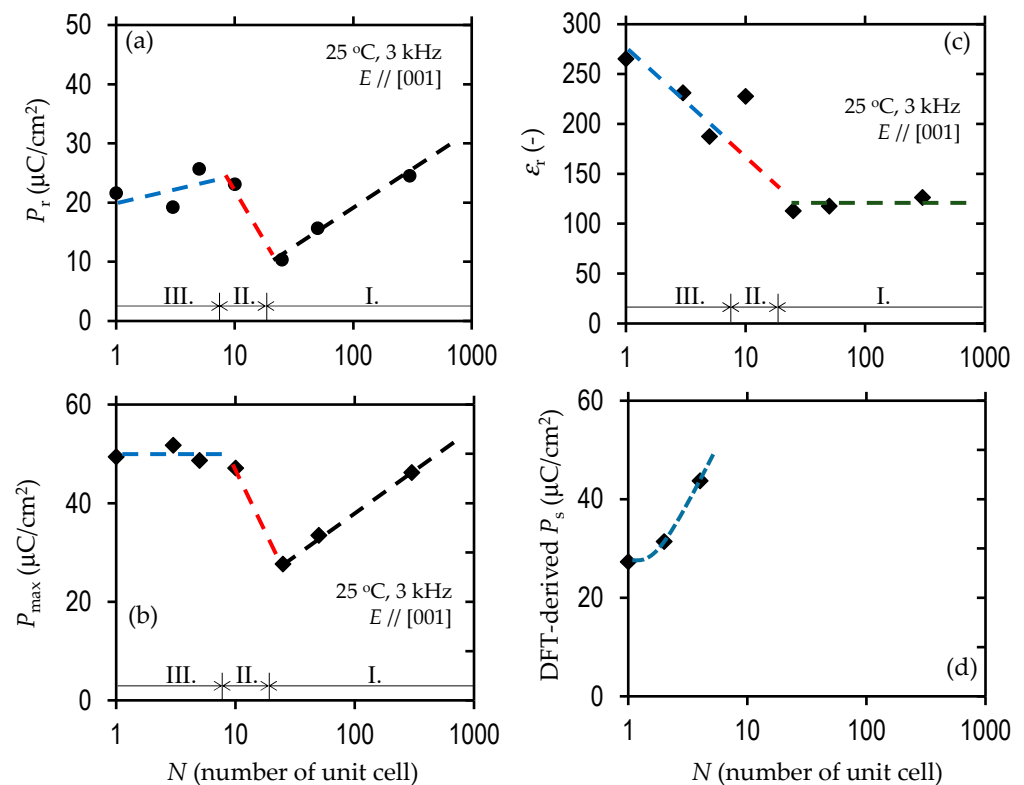
Figure 6. (**a**) Remanent polarization (P_r), (**b**) relative dielectric permittivity (ε_r), (**c**) polarization maximum at the maximum E (P_{max}), and (**d**) spontaneous polarization (P_s) from DFT calculations of the unified unit cells in Figure 2.
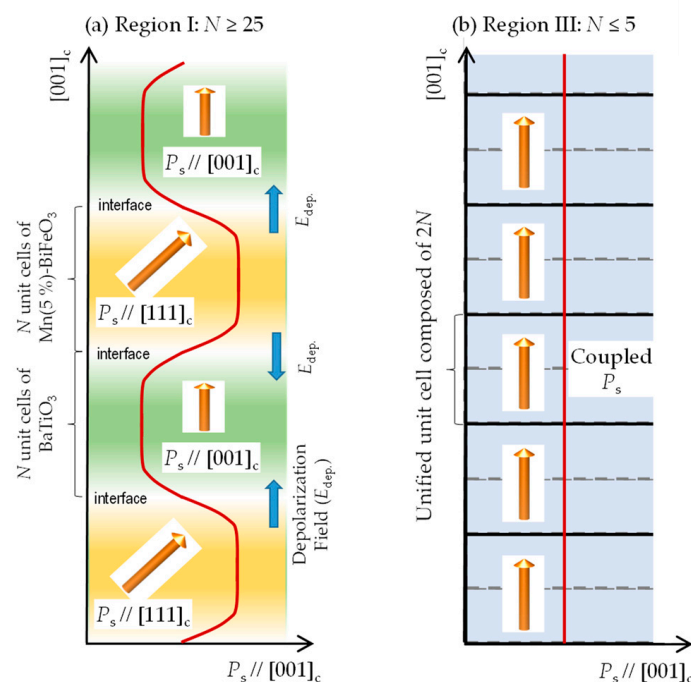
Figure 7. Schematics of the crystal structures of the supercells with (**a**) $N \geq 25$, and (**b**) $N \leq 5$, along with the $[001]_c$ component of P_s. In (**a**), the thickness of the layers of Mn-BiFeO$_3$ and BaTiO$_3$ is sufficiently thin, and thereby their polarization features are maintained inside them. In (**b**), the structural and electronic coupling of Mn-BiFeO$_3$ and BaTiO$_3$ is activated, and the two layers can no longer be distinguished, leading to a unified ferroelectric unit cell.

4. Discussion

Figure 7 shows the schematics of the superlattice structures along with the P_s component along the out-of-plane direction (P_s//$[001]_c$). In region I ($N \geq 25$), the presence of the 1/2 1/2 3/2 reflection from the Mn-BiFeO$_3$ layer (Figure 3) and the polarization and dielectric properties (Figure 6) indicate that the superlattice can be regarded as the simple series connection of the capacitors of BaTiO$_3$ and Mn-BiFeO$_3$. In the BaTiO$_3$ layer, the P_s vector is present along $[001]_c$; our DFT calculations reveal that the P_s strength is 28.5 μC cm^{-2}, which is close to the bulk value [42]. In contrast, the Mn-BiFeO$_3$ layer has a P_s nearly along $[111]_c$, and the value is reported to be 90–100 μC cm^{-2} [37]. As the polarization components along $[001]_c$ in these layers are markedly different, the interface effect plays an important role. It is assumed that the interface region of several to several tens of unit cells in width needs to accommodate the difference in the direction and strength of the P_s vector across it, as in ferroelastic domain walls [43–50]. As a result, a depolarization field ($E_{dep.}$) is built up in the interface region, where the $E_{dep.}$ is present in a direction that prevents the change in the polarization component. Given that the P_s vectors are switched by an E application, the P_r is expected to be ~40 μC cm^{-2}. The P_r of 25 μC cm^{-2} for $N = 300$ is smaller than this expected value, which is caused by a domain clamping by the $E_{dep.}$. In region I, the P_r is reduced when the N is smaller, which is because the volume fraction of the clamped domains is raised by a denser interface with the $E_{dep.}$.

In region III, the 1/2 1/2 3/2 reflection of the Mn-BiFeO$_3$ layer is absent (Figure 3), and the polarization and dielectric properties (Figure 6) cannot be explained by the series connection of the capacitors of BaTiO$_3$ and Mn-BiFeO$_3$. It is reasonable to consider that the superlattice has a unified unit cell, where electronic orbitals of the BaTiO$_3$ and the Mn-BiFeO$_3$ layers are hybridized. In other words, these two layers are no longer distinguished, but the structural and electronic features are completely different from the solid solutions [18]. On the assumption that the superlattice has a unified unit cell (Figure 2), our DFT calculations show that the $N = 1$ cell has a P_s of 27.3 μC cm^{-2}, which is close to the

experimental P_r (21.6 μC cm^{-2}) of $N = 1$. Moreover, the enhancement in P_r with increasing N (Figure 6a) can be qualitatively explained by the theoretical calculations (Figure 6d): P_s is 31.4 μC cm^{-2} for the $N = 2$ cell, and 43.7 μC cm^{-2} for the $N = 4$ cell.

Finally, we comment on an additional degree of freedom in superlattice design by adopting an unequal N in the BaTiO$_3$ and the Mn-BiFeO$_3$ layers, where material properties can be tuned by different N(BaTiO$_3$) and N(Mn-BiFeO$_3$). For example, we can expect that N(BaTiO$_3$) < N(Mn-BiFeO$_3$) delivers an enhanced P_s in a unified cell in the superlattice. Moreover, superlattice design based on different unit cell numbers is anticipated to provide a means to control the strain effect at will.

5. Conclusions

We investigated the crystal structure and dielectric and polarization properties of superlattice-structured epitaxial thin films composed of Mn(5%)-doped BiFeO$_3$ and BaTiO$_3$ with a total thickness of 600 perovskite (ABO$_3$) unit cells. The number of ABO$_3$ unit cell (N) in the layers of Mn-BiFeO$_3$ and BaTiO$_3$ varied from 300 down to 1. It was revealed that the superlattices for an N greater than 25 can be regarded as a simple series connection of their individual capacitors. In the thin regime of an N of five or less, the superlattice behaves as a unified ferroelectric, where the BaTiO$_3$ and Mn-BiFeO$_3$ layers are structurally and electronically coupled. With decreasing N from five to one, the εr is markedly enhanced, whereas the P_r is reduced. DFT calculations show that the P_s is suppressed with decreasing N, which is in good agreement with the experimental P_r. We conclude that superlattices formed by two types of perovskite layers with different crystal symmetries represent a path to novel ferroelectrics that cannot be obtained in a solid solution system.

References

1. Sawaguchi, E. Ferroelectricity versus Antiferroelectricity in the Solid Solutions of PbZrO$_3$ and PbTiO$_3$. *J. Phys. Soc. Jpn.* **1953**, *8*, 615–629. [CrossRef]
2. Jaffe, B.; Roth, R.S.; Marzullo, S. Piezoelectric properties of Lead zirconate-Lead titanate solid-solution ceramics. *J. Appl. Phys.* **1954**, *25*, 809–810. [CrossRef]

3.	Noheda, B.; Gonzalo, J.; Cross, L.; Guo, R.; Park, S. Tetragonal-to-monoclinic phase transition in a ferroelectric perovskite: The structure of $PbZr_{0.52}Ti_{0.48}O_3$. *Phys. Rev. B* **2000**, *61*, 8687–8695. [CrossRef]

4.	Park, S.-E.; Shrout, T.R. Ultrahigh strain and piezoelectric behavior in relaxor based ferroelectric single crystals. *J. Appl. Phys.* **1997**, *82*, 1804. [CrossRef]

5.	Sun, E.; Cao, W. Relaxor-based ferroelectric single crystals: Growth, domain engineering, characterization and applications. *Prog. Mater. Sci.* **2014**, *65*, 124–210. [CrossRef]

6.	Fu, H.; Cohen, R.E. Polarization rotation mechanism for ultrahigh electromechanical response in single-crystal piezoelectrics. *Nature* **2000**, *403*, 281–283. [CrossRef]

7.	Wang, J.; Neaton, J.B.; Zheng, H.; Nagarajan, V.; Ogale, S.B.; Liu, B.; Viehland, D.; Vaithyanathan, V.; Schlom, D.G.; Waghmare, U.V.; et al. Epitaxial $BiFeO_3$ Multiferroic Thin Film Heterostructures. *Science* **2003**, *299*, 1719–1722. [CrossRef]

8.	Fiebig, M. Revival of the magnetoelectric effect. *J. Phys. D Appl. Phys.* **2005**, *38*, R123. [CrossRef]

9.	Ramesh, R.; Spaldin, N.A. Multiferroics: Progress and prospects in thin films. *Nat. Mater.* **2007**, *6*, 21–29. [CrossRef]

10.	Ederer, C.; Spaldin, N.A. Weak ferromagnetism and magnetoelectric coupling in bismuth ferrite. *Phys. Rev. B Condens. Matter Mater. Phys.* **2005**, *71*, 060401(R). [CrossRef]

11.	Michel, C.; Moreau, J.M.; Achenbach, G.D.; Gerson, R.; James, W.J. The atomic structure of $BiFeO_3$. *Solid State Commun.* **1969**, *7*, 701–704. [CrossRef]

12.	Kubel, F.; Schmid, H. Structure of a ferroelectric and ferroelastic monodomain crystal of the perovskite $BiFeO_3$. *Acta Crystallogr. Sect. B Struct. Sci.* **1990**, *46*, 698–702. [CrossRef]

13.	Kumar, M.M.; Srinivas, A.; Suryanarayana, S.V. Structure property relations in $BiFeO_3/BaTiO_3$ solid solutions. *J. Appl. Phys.* **2000**, *87*, 855–862. [CrossRef]

14.	Kitagawa, S.; Ozaki, T.; Horibe, Y.; Yoshii, K.; Mori, S. Ferroelectric domain structures in $BiFeO_3$-$BaTiO_3$. *Ferroelectrics* **2008**, *376*, 122–128. [CrossRef]

15.	Wang, T.H.; Ding, Y.; Tu, C.S.; Yao, Y.D.; Wu, K.T.; Lin, T.C.; Yu, H.H.; Ku, C.S.; Lee, H.Y. Structure, magnetic, and dielectric properties of $(1-x)BiFeO_3$-$xBaTiO_3$ ceramics. *J. Appl. Phys.* **2011**, *109*, 07D907. [CrossRef]

16.	Wei, Y.; Jin, C.; Zeng, Y.; Wang, X.; Xu, G.; Wang, X. Polar Order Evolutions near the Rhombohedral to Pseudocubic and Tetragonal to Pseudocubic Phase Boundaries of the $BiFeO_3$-$BaTiO_3$ System. *Materials* **2015**, *8*, 8355–8365. [CrossRef] [PubMed]

17.	Kim, S.; Khanal, G.P.; Nam, H.W.; Fujii, I.; Ueno, S.; Moriyoshi, C.; Kuroiwa, Y.; Wada, S. Structural and electrical characteristics of potential candidate lead-free $BiFeO_3$-$BaTiO_3$ piezoelectric ceramics. *J. Appl. Phys.* **2017**, *122*, 164105. [CrossRef]

18.	Leontsev, S.O.; Eitel, R.E. Dielectric and Piezoelectric Properties in Mn-Modified $(1-x)BiFeO_3$-$xBaTiO_3$ Ceramics. *J. Am. Ceram. Soc.* **2009**, *92*, 2957–2961. [CrossRef]

19.	Ohtomo, A.; Muller, D.A.; Grazul, J.L.; Hwang, H.Y. Artificial charge-modulation in atomic-scale perovskite titanate superlattices. *Nature* **2002**, *419*, 378–380. [CrossRef]

20.	Lee, H.N.; Christen, H.M.; Chisholm, M.F.; Rouleau, C.M.; Lowndes, D.H. Strong polarization enhancement in asymmetric three-component ferroelectric superlattices. *Nature* **2005**, *433*, 395–399. [CrossRef] [PubMed]

21.	Lorenz, M.; Wagner, G.; Lazenka, V.; Schwinkendorf, P.; Modarresi, H.; Van Bael, M.J.; Vantomme, A.; Temst, K.; Oeckler, O.; Grundmann, M. Correlation of magnetoelectric coupling in multiferroic $BaTiO_3$-$BiFeO_3$ superlattices with oxygen vacancies and antiphase octahedral rotations. *Appl. Phys. Lett.* **2015**, *106*, 012905. [CrossRef]

22.	Lorenz, M.; Lazenka, V.; Schwinkendorf, P.; Van Bael, M.J.; Vantomme, A.; Temst, K.; Grundmann, M.; Höche, T. Epitaxial Coherence at Interfaces as Origin of High Magnetoelectric Coupling in Multiferroic $BaTiO_3$–$BiFeO_3$ Superlattices. *Adv. Mater. Interfaces* **2016**, *3*, 1500822. [CrossRef]

23.	Matsuo, H.; Noguchi, Y.; Miyayama, M.; Kiguchi, T.; Konno, T.J. Enhanced photovoltaic effects in ferroelectric solid solution thin films with nanodomains. *Appl. Phys. Lett.* **2020**, *116*, 132901. [CrossRef]

24.	Hohenberger, S.; Jochum, J.K.; Van Bael, M.J.; Temst, K.; Patzig, C.; Höche, T.; Grundmann, M.; Lorenz, M. Enhanced magneto-electric coupling in $BaTiO_3$-$BiFeO_3$ multilayers-an interface effect. *Materials* **2020**, *13*, 197. [CrossRef]

25.	Hohenberger, S.; Lazenka, V.; Selle, S.; Patzig, C.; Temst, K.; Lorenz, M. Magnetoelectric Coupling in Epitaxial Multiferroic $BiFeO_3$–$BaTiO_3$ Composite Thin Films. *Phys. Status Solidi Basic Res.* **2020**, *257*, 1900613. [CrossRef]

26.	Matsuo, H.; Kitanaka, Y.; Inoue, R.; Noguchi, Y.; Miyayama, M. Cooperative effect of oxygen-vacancy-rich layer and ferroelectric polarization on photovoltaic properties in $BiFeO_3$ thin film capacitors. *Appl. Phys. Lett.* **2016**, *108*, 032901. [CrossRef]

27.	Matsuo, H.; Kitanaka, Y.; Noguchi, Y.; Miyayama, M. Electrical conduction mechanism in $BiFeO_3$-based ferroelectric thin-film capacitors: Impact of Mn doping. *J. Asian Ceram. Soc.* **2015**, *3*, 426–431. [CrossRef]

28.	Noguchi, Y.; Matsuo, H.; Kitanaka, Y.; Miyayama, M. Ferroelectrics with a controlled oxygen-vacancy distribution by design. *Sci. Rep.* **2019**, *9*, 4225. [CrossRef]

29.	Noguchi, Y.; Maki, H.; Kitanaka, Y.; Matsuo, H.; Miyayama, M. Control of misfit strain in ferroelectric $BaTiO_3$ thin-film capacitors with $SrRuO_3$-based electrodes on $(Ba, Sr)TiO_3$-buffered $SrTiO_3$ substrates. *Appl. Phys. Lett.* **2018**, *113*, 012903. [CrossRef]

30.	Matsuo, H.; Noguchi, Y.; Miyayama, M. Gap-state engineering of visible-light-active ferroelectrics for photovoltaic applications. *Nat. Commun.* **2017**, *8*, 207. [CrossRef]

31.	Noguchi, Y.; Tada, M.; Kitanaka, Y.; Miyayama, M. Fabrication and characterization of $(Ba, Sr)RuO_3$ ceramic targets and thin films for ferroelectric $BaTiO_3$ thin-film capacitors. *AIP Adv.* **2018**, *8*, 115135. [CrossRef]

32. Langreth, D.C.; Perdew, J.P. Theory of nonuniform electronic systems. I. Analysis of the gradient approximation and a generalization that works. *Phys. Rev. B* **1980**, *21*, 5469–5493. [CrossRef]

33. Blöchl, P.E. Projector augmented-wave method. *Phys. Rev. B* **1994**, *50*, 17953–17979. [CrossRef]

34. Kresse, G.; Hafner, J. Ab initio molecular-dynamics simulation of the liquid-metal–amorphous-semiconductor transition in germanium. *Phys. Rev. B* **1994**, *49*, 14251–14269. [CrossRef]

35. Perdew, J.P.; Ruzsinszky, A.; Csonka, G.I.; Vydrov, O.A.; Scuseria, G.E.; Constantin, L.A.; Zhou, X.; Burke, K. Restoring the Density-Gradient Expansion for Exchange in Solids and Surfaces. *Phys. Rev. Lett.* **2008**, *100*, 136406. [CrossRef]

36. Anisimov, V.I.; Zaanen, J.; Andersen, O.K. Band theory and Mott insulators: Hubbard *U* instead of Stoner *I*. *Phys. Rev. B* **1991**, *44*, 943–954. [CrossRef]

37. Neaton, J.B.; Ederer, C.; Waghmare, U.V.; Spaldin, N.A.; Rabe, K.M. First-principles study of spontaneous polarization in multiferroic $BiFeO_3$. *Phys. Rev. B* **2005**, *71*, 014113. [CrossRef]

38. Gonze, X.; Lee, C. Dynamical matrices, Born effective charges, dielectric permittivity tensors, and interatomic force constants from density-functional perturbation theory. *Phys. Rev. B Condens. Matter Mater. Phys.* **1997**, *55*, 10355–10368. [CrossRef]

39. Chen, Z.; Qi, Y.; You, L.; Yang, P.; Huang, C.W.; Wang, J.; Sritharan, T.; Chen, L. Large tensile-strain-induced monoclinic M_B phase in $BiFeO_3$ epitaxial thin films on a $PrScO_3$ substrate. *Phys. Rev. B Condens. Matter Mater. Phys.* **2013**, *88*, 054114. [CrossRef]

40. Zubko, P.; Catalan, G.; Tagantsev, A.K. Flexoelectric effect in solids. *Annu. Rev. Mater. Res.* **2013**, *43*, 387–421. [CrossRef]

41. Maki, H.; Noguchi, Y.; Kutsuna, K.; Matsuo, H.; Kitanaka, Y.; Miyayama, M. Crystal structure and polarization hysteresis properties of ferroelectric BaTiO 3 thin-film capacitors on $(Ba,Sr)TiO_3$-buffered substrates. *Jpn. J. Appl. Phys.* **2016**, *55*, 10TA03. [CrossRef]

42. Imura, R.; Kitanaka, Y.; Oguchi, T.; Noguchi, Y.; Miyayama, M. Polarization properties and crystal structures of ferroelectric $(Ba,Ca)TiO_3$ single crystals. *J. Adv. Dielectr.* **2014**, *04*, 1450003. [CrossRef]

43. Meyer, B.; Vanderbilt, D. Ab initio study of ferroelectric domain walls in $PbTiO_3$. *Phys. Rev. B* **2002**, *65*, 104111. [CrossRef]

44. Catalan, G.; Seidel, J.; Ramesh, R.; Scott, J.F. Domain wall nanoelectronics. *Rev. Mod. Phys.* **2012**, *84*, 119–156. [CrossRef]

45. Farokhipoor, S.; Noheda, B. Conduction through 71° Domain Walls in $BiFeO_3$ Thin Films. *Phys. Rev. Lett.* **2011**, *107*, 127601. [CrossRef]

46. Dennis, M.D.; Bradt, R.C. Thickness of 90° ferroelectric domain walls in $(Ba,Pb)TiO_3$ single crystals. *J. Appl. Phys.* **1974**, *45*, 1931–1933. [CrossRef]

47. Yang, S.Y.; Seidel, J.; Byrnes, S.J.; Shafer, P.; Yang, C.-H.; Rossell, M.D.; Yu, P.; Chu, Y.-H.; Scott, J.F.; Ager, J.W.; et al. Above-bandgap voltages from ferroelectric photovoltaic devices. *Nat. Nanotechnol.* **2010**, *5*, 143–147. [CrossRef]

48. Inoue, R.; Ishikawa, S.; Imura, R.; Kitanaka, Y.; Oguchi, T.; Noguchi, Y.; Miyayama, M. Giant photovoltaic effect of ferroelectric domain walls in perovskite single crystals. *Sci. Rep.* **2015**, *5*, 14741. [CrossRef]

49. Matsuo, H.; Kitanaka, Y.; Inoue, R.; Noguchi, Y.; Miyayama, M.; Kiguchi, T.; Konno, T.J.T.J. Bulk and domain-wall effects in ferroelectric photovoltaics. *Phys. Rev. B* **2016**, *94*, 214111. [CrossRef]

50. Noguchi, Y.; Inoue, R.; Matsuo, H. Domain-wall photovoltaic effect in Fe-doped $BaTiO_3$ single crystals. *J. Appl. Phys.* **2021**, *129*, 084101. [CrossRef]